aerospace

MDPI

Article

Reduced-Order Modeling of Sweeping Jet Actuators Using Eigenvalue-Sorted Dynamic Mode Decomposition

Shafi Al Salman Romeo, Mobashera Alam and Kursat Kara *

School of Mechanical and Aerospace Engineering, Oklahoma State University, Stillwater, OK 74078, USA; sromeo@okstate.edu (S.A.S.R.); mobashera.alam@okstate.edu (M.A.)
* Correspondence: kursat.kara@okstate.edu

Abstract

Sweeping jet actuators (SJAs) are promising for active flow control in aerospace systems, but integrating actuator-resolved unsteady CFD into full-configuration simulations is often impractical due to small geometric scales and $\mathcal{O}(10^2)$ Hz oscillations that demand fine grids and small time steps. This work develops a reduced-order modeling (ROM) framework to generate time-resolved boundary conditions at the actuator exit from SJA flow data. Dynamic mode decomposition (DMD) is particularly attractive for this purpose because it provides a linear, data-driven input–output representation of the actuator effect, even though it does not explicitly model the underlying nonlinear switching mechanism. We introduce an eigenvalue-sorted dynamic mode decomposition (ES-DMD) method that performs stability-aware mode ranking based on the discrete-time DMD eigenvalues, prioritizing modes with $\Re(\lambda)$ closest to unity to retain near-neutrally stable oscillatory dynamics, improving robustness relative to conventional amplitude-based selections for high-frequency oscillatory flows. The method is evaluated across multiple operating conditions, with detailed analysis performed for the highest mass-flow case ($\dot{m} = 0.01$ lb/s), representing the most dynamically demanding condition considered. Across multiple operating conditions, ES-DMD yields consistent reconstructions of the dominant switching dynamics. For one-dimensional exit-plane profiles, combining ES-DMD with time-delay embedding enables accurate reconstruction and multi-period prediction using only 20 modes (7.6% of the full system rank). The proposed approach provides a practical pathway to incorporate unsteady SJA effects into large-scale aerospace CFD through compact, predictive boundary-condition models.

Keywords: active flow control; sweeping jet actuator; reduced-order modeling; dynamic mode decomposition; boundary condition; computational fluid dynamics; eigenvalue sorting; stability-aware mode selection; time-delay embedding

Check for updates

Academic Editor: Lawrence S. Ukeiley

Received: 17 December 2025
Revised: 12 February 2026
Accepted: 13 February 2026
Published: 17 February 2026

Copyright: © 2026 by the authors. Licensee MDPI, Basel, Switzerland. This article is an open access article distributed under the terms and conditions of the Creative Commons Attribution (CC BY) license.

1. Introduction

Active flow control (AFC) using fluidic actuators has attracted sustained interest in aerospace applications due to its potential to improve aerodynamic performance, including drag reduction, lift enhancement, and separation control [1–3]. Among these devices, sweeping jet actuators (SJAs) are particularly appealing because they generate self-sustaining, high-amplitude oscillatory jets without moving parts, offering robustness and mechanical simplicity [4,5]. These characteristics make SJAs attractive for integration into wings, control surfaces, and propulsion–airframe interaction concepts [6–8].

Despite their promise, the widespread use of SJAs in full-scale aerospace simulations remains limited [9,10]. The primary barrier is computational. Internal SJA flows involve small geometric features and oscillations typically in the $\mathcal{O}(10^2)$ Hz range, which require actuator-resolved grids and time steps on the order of 10^{-5}–10^{-4} s [11–13]. When embedded into global aircraft simulations that otherwise employ Reynolds-Averaged Navier–Stokes (RANS) models with much larger time steps, even a single actuator can increase computational cost by orders of magnitude [14,15]. Simulating arrays of SJAs, as required for practical AFC strategies, quickly becomes intractable [16,17].

A practical alternative is to decouple actuator-scale dynamics from the global flow solution by representing the actuator through a reduced-order model (ROM) [18]. In this paradigm, high-fidelity simulations or experiments are used once to characterize the actuator behavior, and the resulting ROM supplies time-resolved boundary conditions (e.g., velocity or pressure profiles) to the larger-scale simulation [19,20]. The central challenge is to construct a ROM that is both compact and capable of reproducing the actuator's unsteady switching dynamics.

Dynamic Mode Decomposition (DMD) provides a data-driven framework for extracting coherent spatio-temporal structures from time-resolved flow fields [21,22]. Unlike modal decompositions that focus purely on energetic content, DMD yields a linear dynamical system approximation of the observed flow evolution, effectively modeling the actuator's input–output effect rather than explicitly resolving the underlying nonlinear switching mechanism. This linear representation does not imply that the SJA dynamics are linear; rather, it provides a locally optimal linear approximation of the measured nonlinear evolution over the sampled time window. DMD has been successfully applied to a wide range of aerodynamic flows, including wakes, cavities, and oscillatory jets [23,24]. Recent studies have applied DMD-type analyses to fluidic and synthetic jet configurations, demonstrating its suitability for oscillatory jet dynamics; however, its specific application to sweeping jet actuator boundary-condition modeling and reduced-order propagation remains comparatively limited. For periodic systems such as SJAs, DMD naturally identifies modes associated with dominant oscillation frequencies [25,26].

Alternative modal approaches such as Proper Orthogonal Decomposition (POD) and Spectral POD (SPOD) provide energetically optimal and frequency-resolved structures that are valuable for flow diagnostics [27,28]. However, these approaches do not directly yield an explicit reduced linear evolution operator for time advancement. In contrast, DMD produces a finite-dimensional linear propagator that can be evaluated recursively, which is essential for generating time-resolved boundary conditions within coupled RANS simulations. For ROM deployment rather than modal interpretation, this predictive capability motivates the use of DMD over purely energy-based decompositions.

However, standard DMD mode selection strategies, which rely on singular value truncation or amplitude ranking, can be sensitive to noise and may fail to capture switching dynamics in high-frequency oscillatory flows [29–31].

Time-delay embedding has been shown to improve DMD prediction by enriching temporal information, particularly for low-dimensional or sparsely sampled data [32,33]. While effective, time-delay embedding increases the effective state dimension and can become expensive when applied directly to high-resolution two- or three-dimensional datasets. For aerospace applications, where the quantity of interest is often a one-dimensional exit-plane profile rather than the full internal flow, an efficient combination of mode selection and temporal embedding is required.

To address these challenges, this work proposes an Eigenvalue-Sorted Dynamic Mode Decomposition (ES-DMD) framework tailored for high-frequency sweeping jet actuators. The finalized sorting criterion ranks modes using the real part of the discrete-time DMD

eigenvalues, $I = \Re(\lambda)$, thereby prioritizing modes clustered near the unit circle and close to $\lambda \approx 1$, which correspond to near-neutrally stable oscillatory dynamics governing sustained jet switching. This stability-aware eigenvalue-based sorting improves robustness over conventional amplitude-based selections by systematically suppressing decaying transient modes rapidly. The approach is first validated using two-dimensional unsteady CFD data across multiple operating conditions. Its primary aerospace application is then demonstrated by combining ES-DMD with time-delay embedding to construct a compact, predictive ROM for one-dimensional exit-plane profiles. The resulting model provides accurate, time-resolved boundary conditions using a small number of modes, enabling efficient multiscale simulations of SJA-integrated aerospace configurations.

The remainder of the paper is organized as follows. Section 2 describes the numerical model and its validation. Section 3 presents the DMD formulation, the proposed ES-DMD method, and the incorporation of time-delay embedding. Section 4 evaluates the method's performance across operating conditions and demonstrates its use for boundary-condition generation. Section 5 summarizes the findings and discusses implications for aerospace active flow control simulations.

2. Numerical Model and Validation

The flow data used for reduced-order modeling were obtained from a two-dimensional unsteady Reynolds-Averaged Navier–Stokes (URANS) simulation of a canonical SJA. The objective of the computational model is not to resolve all three-dimensional turbulent features of the actuator, but to provide a reliable, time-resolved dataset that captures the dominant oscillatory dynamics required to develop and evaluate the proposed reduced-order modeling framework. The primary goal of the present study is boundary-condition generation rather than turbulence-resolving flow physics; therefore, accurately reproducing switching frequency, jet deflection, and exit-plane velocity dynamics is prioritized over resolving fine-scale turbulence structures. This modeling philosophy is consistent with prior SJA studies that employ two-dimensional URANS to analyze oscillation frequency, jet switching behavior, and exit-plane dynamics relevant to boundary-condition modeling [34–36].

Higher-fidelity approaches such as LES, DES, or DDES can capture additional three-dimensional turbulence features; however, their computational cost increases substantially, particularly when resolving actuator internal geometry and high-frequency oscillations. Since the present reduced-order modeling framework relies primarily on coherent switching dynamics and exit-plane signals, two-dimensional URANS provides a computationally efficient and sufficiently accurate dataset for ROM development while maintaining consistency with the intended RANS-based aerospace integration environment.

2.1. Geometry, Mesh, and Solver Configuration

The SJA geometry follows a well-established configuration with a nozzle throat height of $h = 6.35$ mm, consistent with previous numerical and experimental investigations [13,34]. The computational domain extends sufficiently downstream of the actuator exit to capture the oscillating jet in a quiescent environment, as illustrated in Figure 1. A structured–unstructured hybrid mesh is employed, with local refinement in the throat and exit regions to resolve shear layers and switching dynamics.

The mesh corresponds to the validated N-60 configuration reported by Alam et al. [36], consisting of approximately 4×10^5 cells. Ten inflation layers are applied along solid walls, ensuring near-wall resolution of $y^+ < 1$. A mesh independence study conducted in the reference work demonstrated less than 5.5% variation in mean flow quantities and negligible differences in oscillation frequency compared to a finer N-80 mesh, confirming grid convergence for the quantities of interest. The selected 4×10^5-cell mesh therefore

represents a balance between computational efficiency and adequate resolution of shear-layer gradients and switching dynamics, which are critical for accurate modal extraction.

All simulations were performed using ANSYS Fluent 2021.R2 [37]. The compressible flow was solved using the pressure-based coupled algorithm with second-order spatial discretization for all flow variables. Temporal integration employed a bounded second-order implicit scheme. Turbulence closure was provided by the Shear Stress Transport (SST) k–ω model [38]. Convergence was monitored by requiring that the residuals for all governing equations fall below 10^{-6} at each time step.

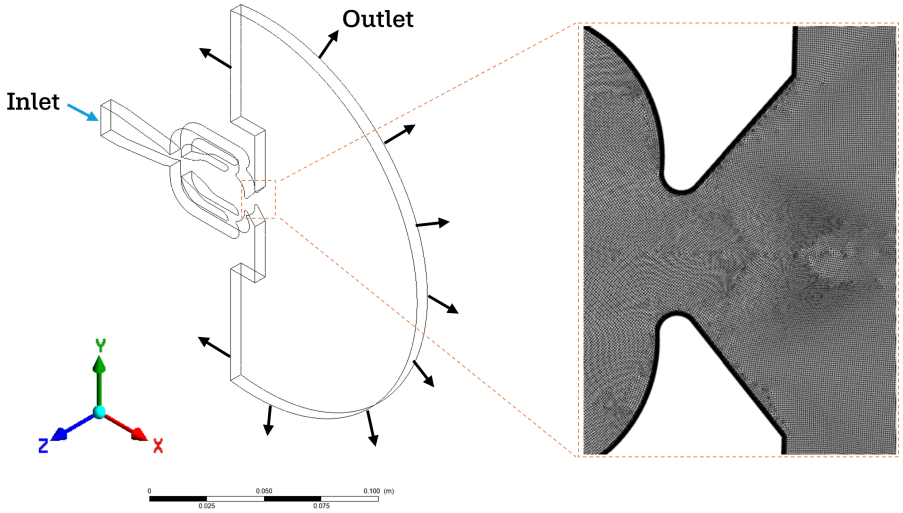


Figure 1. (**Left**) Computational domain of the SJA showing the inlet, outlet, and the extended region for capturing the oscillating jet in a quiescent environment. (**Right**) Close-up view of the mesh in the nozzle exit region.

2.2. Boundary Conditions and Operating Cases

A mass-flow inlet boundary condition was prescribed at the actuator supply, while the external domain boundaries were treated as pressure outlets at standard atmospheric conditions (101,325 Pa, 300 K). The working fluid was air, modeled as an ideal gas, with molecular viscosity computed using Sutherland's law. Three inlet mass flow rates were considered to span a representative range of oscillation frequencies as listed in Table 1. The highest mass-flow case (Case 3) is later selected as the primary baseline for detailed modal analysis, as it represents the most dynamically demanding operating condition considered.

Table 1. SJA Operating Conditions for ROM Development.

Case	Mass Flow Rate	Frequency	Strouhal Number	Exit Mach
1	0.0025 lb/s (1.13×10^{-3} kg/s)	65.9 Hz	0.040	0.09
2	0.005 lb/s (2.27×10^{-3} kg/s)	131.8 Hz	0.018	0.17
3 (Baseline)	0.01 lb/s (4.54×10^{-3} kg/s)	263.5 Hz	0.014	0.34

The Strouhal number is defined as $St = fh/U_j$, where U_j is the mean velocity at the nozzle throat.

Time steps in the range 2×10^{-5}–1×10^{-4} s were used to resolve the actuator oscillations while maintaining numerical stability. Based on the mean throat velocity and throat height $h = 6.35$ mm, the corresponding Reynolds numbers range approximately from $Re_h \approx 2 \times 10^4$ (Case 1) to $Re_h \approx 1 \times 10^5$ (Case 3), placing the internal jet flow within the transitional to turbulent regime typical of practical SJAs.

2.3. Model Validation and Applicability

The credibility of the reduced-order modeling results depends on the fidelity of the underlying CFD data. The numerical setup adopted here has been validated in prior work against experimental measurements. Specifically, Alam et al. [36] reported that a two-dimensional URANS simulation using the same geometry, mesh strategy, and solver configuration predicted an oscillation frequency of 350.04 Hz at a mass flow rate of 0.015 lb/s, within 3.64% of the experimentally measured value of 337.70 Hz reported by Slupski et al. [13]. This prediction is also consistent with three-dimensional URANS results, which exhibited a 1.21% deviation [39].

Although three-dimensional effects are present in practical sweeping jet actuators, prior studies have shown that two-dimensional URANS captures the dominant bistable oscillation mechanism and frequency scaling with sufficient accuracy for reduced-order modeling and boundary-condition development [34,35]. In the present work, the two-dimensional model is employed as a computationally efficient, validated data source to develop the ES-DMD framework. The emphasis is on reproducing temporal switching behavior and exit-plane dynamics rather than detailed three-dimensional turbulence statistics. The maximum exit Mach number considered in this study is 0.34. While higher-Mach-number SJAs (e.g., $M \approx 0.6$ or near-sonic conditions) may introduce stronger compressibility effects and sharper gradients, the present framework is data-driven and therefore extensible to higher Mach numbers provided that appropriate training data are available. As shown later in Section 4, the increase in modal content at higher frequencies indicates that additional retained modes would be required to maintain comparable reconstruction accuracy in more aggressive operating regimes.

This modeling choice aligns with the intended aerospace application of the proposed ROM: supplying time-resolved actuator boundary conditions to large-scale RANS simulations, where resolving full actuator geometry and internal turbulence would be prohibitively expensive. Extensions to three-dimensional simulations and higher-fidelity datasets are discussed as part of future work.

3. Methodology

This section presents the reduced-order modeling framework used in this study. First, the standard DMD formulation is briefly reviewed to establish notation. The proposed Eigenvalue-Sorted DMD (ES-DMD) method is then introduced, emphasizing its stability-aware mode selection strategy for high-frequency oscillatory systems. Finally, the integration of time-delay embedding for predicting one-dimensional exit-plane profiles is described.

3.1. Standard Dynamic Mode Decomposition

DMD is a data-driven technique that approximates the Koopman operator to extract coherent spatio-temporal structures from time-resolved data [21,22]. Consider a sequence of flow snapshots

$$\mathbf{x}^k \in \mathbb{R}^n, \quad k = 1, 2, \ldots, m,$$

sampled at uniform time intervals Δt. These snapshots are arranged into two data matrices:

$$\mathbf{X} = [\mathbf{x}^1, \mathbf{x}^2, \ldots, \mathbf{x}^{m-1}], \quad \mathbf{X}' = [\mathbf{x}^2, \mathbf{x}^3, \ldots, \mathbf{x}^m].$$

DMD assumes the existence of a linear operator $\mathbf{A}$ such that

$$\mathbf{X}' \approx \mathbf{A}\mathbf{X}.$$

Since $\mathbf{A}$ is generally high-dimensional, a low-rank approximation is obtained via Singular Value Decomposition (SVD) of $\mathbf{X}$:

$$\mathbf{X} \approx \mathbf{U}_r \mathbf{\Sigma}_r \mathbf{V}_r^*,$$

where r is the truncated rank based on singular value decay. The reduced-order operator is then

$$\tilde{\mathbf{A}} = \mathbf{U}_r^* \mathbf{X}' \mathbf{V}_r \mathbf{\Sigma}_r^{-1}.$$

An eigendecomposition of $\tilde{\mathbf{A}}$ yields eigenvalues λ_j and eigenvectors $\mathbf{w}_j$:

$$\tilde{\mathbf{A}} \mathbf{w}_j = \lambda_j \mathbf{w}_j.$$

The corresponding DMD modes are

$$\boldsymbol{\phi}_j = \mathbf{U}_r \mathbf{w}_j.$$

To interpret the dynamics in continuous time, the discrete-time eigenvalues are mapped as

$$\alpha_j = \frac{\ln(\lambda_j)}{\Delta t},$$

where $\Re(\alpha_j)$ represents the exponential growth or decay rate, and $\Im(\alpha_j)$ represents the oscillation frequency of the mode.

The flow field at time t is reconstructed as

$$\mathbf{x}_{\mathrm{DMD}}(t) = \sum_{j=1}^{r} b_j \boldsymbol{\phi}_j e^{\alpha_j t}, \tag{1}$$

where the modal amplitudes $\mathbf{b}$ are obtained via least-squares projection of the initial condition:

$$\mathbf{b} = \mathbf{\Phi}^{\dagger} \mathbf{x}^1,$$

with $\mathbf{\Phi} = [\boldsymbol{\phi}_1, \ldots, \boldsymbol{\phi}_r]$ and $\dagger$ denoting the Moore–Penrose pseudoinverse.

Standard Dynamic Mode Decomposition commonly relies on truncation based on singular values or on ranking modes by their initial amplitudes $|b_j|$. While effective for many flows, amplitude-based selection can be unreliable for high-frequency oscillatory systems such as sweeping jet actuators, where dynamically important switching behavior may not correspond to the largest initial modal amplitudes [40–42].

3.2. Eigenvalue-Sorted Dynamic Mode Decomposition (ES-DMD)

To improve robustness, we introduce an Eigenvalue-Sorted Dynamic Mode Decomposition (ES-DMD) approach that prioritizes modes based on the properties of their discrete-time eigenvalues. Rather than ranking modes using modal amplitude or continuous-time decay rates, the finalized sorting criterion is defined directly in discrete time as

$$I_j = \Re(\lambda_j), \tag{2}$$

where λ_j are the discrete-time DMD eigenvalues.

Modes are sorted in descending order of I_j, thereby prioritizing eigenvalues whose real parts are closest to unity. For oscillatory actuator flows, eigenvalues associated with sustained switching dynamics lie near the unit circle, and their real parts approach one. This criterion therefore emphasizes near-neutrally stable oscillatory modes while systematically deprioritizing rapidly decaying transient components.

In practice, ES-DMD ranking is applied after SVD truncation to rank r, so the low-rank projection already suppresses spurious low-energy modes.

This discrete-time stability-aware sorting emphasizes persistent oscillatory content without explicitly imposing amplitude weighting or frequency filtering. As a result, ES-DMD preferentially retains modes governing sustained jet switching while avoiding transient modes that decay quickly or introduce reconstruction artifacts.

After sorting, the top $k \leq r$ modes are retained for reconstruction and prediction. The resulting ES-DMD approximation of the flow field follows the same reconstruction form as Equation (1), but using the eigenvalue-sorted ordering of modes:

$$\mathbf{x}_{\text{ES-DMD}}(t) = \sum_{j=1}^{k} b_{ES_j} \boldsymbol{\phi}_{\boldsymbol{ES}_j} e^{\alpha_{ES_j} t}. \tag{3}$$

This procedure is summarized in Algorithm 1.

Algorithm 1 Eigenvalue-Sorted Dynamic Mode Decomposition (ES-DMD)

1: **Input:** Snapshot matrices $\mathbf{X}, \mathbf{X}'$, truncation rank r, retained modes $k \leq r$, time step Δt
2: **Output:** Selected DMD modes $\boldsymbol{\Phi}_{\text{ES}}$, eigenvalues $\boldsymbol{\lambda}_{\text{ES}}$, modal amplitudes $\mathbf{b}_{\text{ES}}$
3: Perform Singular Value Decomposition:

$$\mathbf{X} \approx \mathbf{U}_r \boldsymbol{\Sigma}_r \mathbf{V}_r^*$$

4: Compute reduced-order operator:

$$\tilde{\mathbf{A}} = \mathbf{U}_r^* \mathbf{X}' \mathbf{V}_r \boldsymbol{\Sigma}_r^{-1}$$

5: Compute eigendecomposition:

$$\tilde{\mathbf{A}}\mathbf{W} = \mathbf{W}\boldsymbol{\Lambda}$$

6: Compute DMD modes:

$$\boldsymbol{\Phi} = \mathbf{U}_r \mathbf{W}$$

7: Compute modal amplitudes:

$$\mathbf{b} = \boldsymbol{\Phi}^{\dagger} \mathbf{x}^1$$

8: Define sorting index using discrete-time eigenvalues:

$$I_j = \Re(\lambda_j)$$

9: Sort indices in descending order of I_j
10: Retain top k modes to form $\boldsymbol{\Phi}_{\text{ES}}$ and $\mathbf{b}_{\text{ES}}$

It is emphasized that the continuous-time mapping α_j is used solely for reconstruction and interpretation of growth rates and frequencies, while mode selection is performed entirely in discrete time.

3.3. Time-Delay Embedding for Exit-Plane Profile Prediction

For aerospace applications, the primary quantity of interest is often the time-varying velocity or pressure profile at the actuator exit, rather than the full internal flow field. These profiles are typically one-dimensional and contain limited spatial information, which can reduce the robustness of standard DMD predictions.

In the present context, reconstruction refers to reproducing the data used to build the reduced-order model within the training window, whereas prediction refers to advancing the model state beyond the final snapshot of the training dataset.

To enrich the temporal dynamics, time-delay embedding is employed for one-dimensional profile data. Given a sequence of snapshots $\{\mathbf{x}^1, \ldots, \mathbf{x}^m\}$, a Hankel matrix [43] with l delays is constructed as

$$\mathbf{H} = \begin{bmatrix} \mathbf{x}^1 & \mathbf{x}^2 & \cdots & \mathbf{x}^{m-l+1} \\ \mathbf{x}^2 & \mathbf{x}^3 & \cdots & \mathbf{x}^{m-l+2} \\ \vdots & \vdots & \ddots & \vdots \\ \mathbf{x}^l & \mathbf{x}^{l+1} & \cdots & \mathbf{x}^m \end{bmatrix}.$$

Each column of $\mathbf{H}$ represents a temporally augmented state vector containing l consecutive samples of the exit-plane signal. This embedding increases the effective state dimension while preserving the linear DMD framework, enabling the model to approximate higher-order temporal correlations associated with nonlinear jet switching.

The DMD formulation is then applied to the delayed data matrices $\mathbf{H}^1$ and $\mathbf{H}^2$, replacing $\mathbf{X}$ and $\mathbf{X}'$.

Time-delay embedding increases the effective state dimension and exposes higher-order temporal correlations, often yielding a more accurate linear approximation of the underlying nonlinear dynamics [44,45]. Although the actuator switching mechanism is inherently nonlinear, the augmented linear model constructed through delay embedding captures its dominant periodic structure over multiple cycles, which is sufficient for boundary-condition generation in coupled simulations.

When combined with ES-DMD, this approach enables stable multi-period prediction of exit-plane profiles using a small number of retained modes. This efficiency is particularly important for multiscale aerospace simulations, where the reduced-order model is evaluated repeatedly at each global RANS time step to supply time-resolved actuator boundary conditions.

4. Results

The performance of the proposed ES-DMD framework is evaluated using the sampling strategy illustrated in Figure 2. The analysis proceeds in four stages. First, ES-DMD is compared with commonly used DMD mode-selection criteria for high-frequency SJA flows. Second, the method's sensitivity to temporal discretization is assessed. Third, the robustness of ES-DMD across a range of operating frequencies is demonstrated. Finally, the primary aerospace application of the method, the generation of compact, predictive boundary conditions from one-dimensional exit-plane profiles, is presented.

4.1. Comparison of DMD Mode Selection Criteria

The selection of dynamically relevant modes is a critical step in reduced-order modeling of oscillatory flows [46]. In high-frequency SJA systems, amplitude-based truncation can under-represent switching behavior when the corresponding dynamics are not associated with the largest initial modal amplitudes. To quantify the impact of different selection strategies, four mode-ranking criteria are compared using the high-mass-flow operating condition ($\dot{m} = 0.01$ lb/s, $f = 263.5$ Hz, exit Mach 0.34), which serves as the baseline case for the following full-field comparisons.

All comparisons use identical parameters: truncation rank $r = 150$ (approximately 50% of the full system rank), time step $\Delta t = 5 \times 10^{-5}$ s, and 800 snapshots spanning multiple oscillation periods. This relatively large retained rank is intentionally chosen to isolate the effect of the sorting criteria rather than to rely on aggressive truncation.

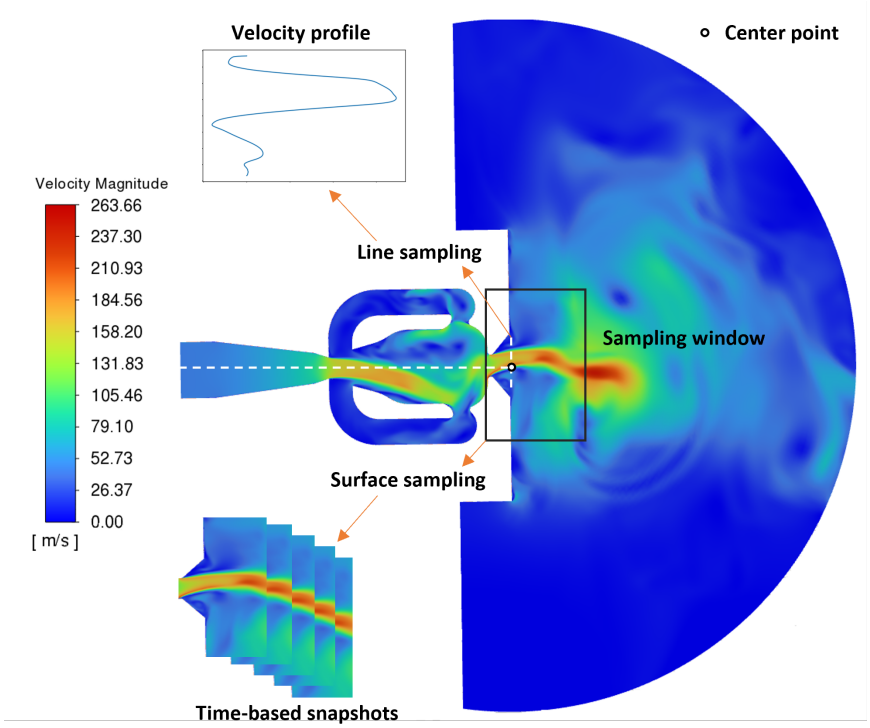


Figure 2. Schematic of the sweeping jet actuator geometry and data sampling strategy. Two-dimensional surface data within the sampling window are used for full-field DMD analysis. One-dimensional line sampling data at the exit interface (dashed white line) are used to generate boundary conditions. The center point $(0, 0)$ is selected for pointwise temporal analysis of velocity and pressure.

Four reconstruction strategies are considered and compared:

Criterion S1: Amplitude-based sorting

$$I_i = |b_i| \tag{4}$$

Using modes approximately 60% of the cumulative weight function (discussed later in Figure 3), amplitude-based sorting captures the mean jet structure. Still, it underestimates peak velocities in the shear layers. The resulting absolute error remains noticeable in the shear-layer and switching region, indicating reduced fidelity in capturing extrema that are central to SJA dynamics at higher frequency.

Criterion S2: Amplitude weighted by growth/decay

$$I_i = |b_i|\left(e^{-\sigma_i} + e^{\sigma_i}\right) \tag{5}$$

where $\sigma_i = \Re(\alpha_i)$. Although this criterion incorporates stability information, it produces spatial overshoots and localized unphysical fluctuations. For the present baseline case, these artifacts appear as patchy regions and amplified errors in the near-exit and shear-layer zones, consistent with sensitivity to transient contributions that do not persist over multiple oscillation cycles.

Criterion S3: Amplitude integrated over time

$$I_i = |b_i|\frac{e^{\sigma_i T} - 1}{\sigma_i T} \tag{6}$$

This criterion emphasizes long-time contributions while suppressing oscillatory switching components. It is important to clarify that Criterion S3 does not necessarily yield unstable or poor reconstructions. Because it weights modes by their time-integrated contributions, S3 often produces relatively smooth spatial fields. However, in the present high-frequency baseline case, this smoothing effect is accompanied by a reduction in the sharpness of the switching-driven gradients near the nozzle exit. While the overall jet structure remains coherent, peak amplitudes and rapid deflection dynamics are comparatively damped. For boundary-condition generation, where accurate representation of extrema and phase-sensitive oscillatory behavior is critical, emphasizing long-time integrated magnitude alone is insufficient.

Criterion S4: Proposed ES-DMD (stability-aware sorting)

ES-DMD ranks modes using the stability-aware index defined in Section 3 (Equation (2)), applied after SVD truncation to rank r. The sorting index is defined directly in discrete time as

$$I_j = \Re(\lambda_j),$$

where λ_j are the discrete-time DMD eigenvalues. This criterion prioritizes modes whose eigenvalues have real parts closest to unity, typically clustered near the unit circle in the complex plane. Such eigenvalues correspond to near-neutrally stable oscillatory dynamics that persist over multiple switching cycles. By emphasizing sustained components rather than transient or rapidly decaying modes, ES-DMD better captures the SJA's dominant switching behavior. The low-rank SVD projection further suppresses low-energy numerical modes before eigenvalue-based sorting is applied.

A cumulative weight function κ is used to characterize the retained modal content:

$$\beta_i = \sqrt{|b_i|}, \qquad \kappa = \frac{\sum_{j=1}^{n} \sum_{i=1}^{j} \beta_i}{\sum_{i=1}^{n} \beta_i}, \tag{7}$$

where b_i denotes the DMD modal amplitudes. Figure 3 compares the cumulative modal weight κ for the four mode-ranking strategies. For a fixed truncation $r = 150$, the retained cumulative weight differs across criteria: S1 retains the largest κ, followed by S2, S3, and S4. It indicates that amplitude-based sorting (S1) accumulates energetic contributions more rapidly, while eigenvalue-based sorting (S4) distributes modal weight more evenly across the spectrum.

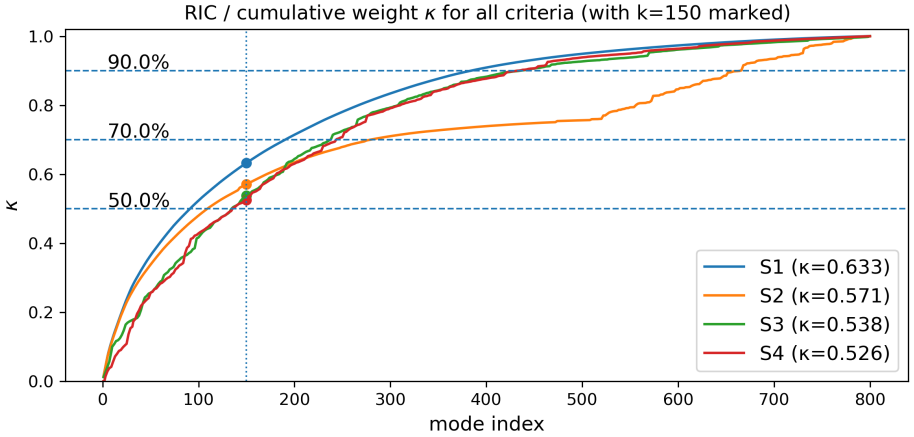


Figure 3. Cumulative modal weight κ (RIC) as a function of sorted mode index for the four selection criteria (S1–S4) for the baseline case ($\dot{m} = 0.01$ lb/s). The vertical dotted line marks $r = 150$. The colored circles indicate the value of κ at $r = 150$ for each criterion. Horizontal dashed lines indicate representative thresholds (50%, 70%, and 90%).

Importantly, a higher cumulative weight does not necessarily imply improved reconstruction of switching dynamics. While S1 reaches larger κ values at $r = 150$, later comparisons in Figure 4 show that ES-DMD (S4), despite slightly lower cumulative weight at the same truncation, yields a more physically consistent reconstruction of the high-frequency switching structures. This distinction highlights that energy-based accumulation alone is insufficient for capturing dynamically persistent oscillatory behavior in high-frequency SJAs.

Reconstruction accuracy is quantified using the normalized absolute error

$$\mathrm{abs}(E_i) = \left| \frac{\mathrm{CFD}_i}{\max(\mathrm{CFD})} - \frac{\mathrm{DMD}_i}{\max(\mathrm{DMD})} \right|. \tag{8}$$

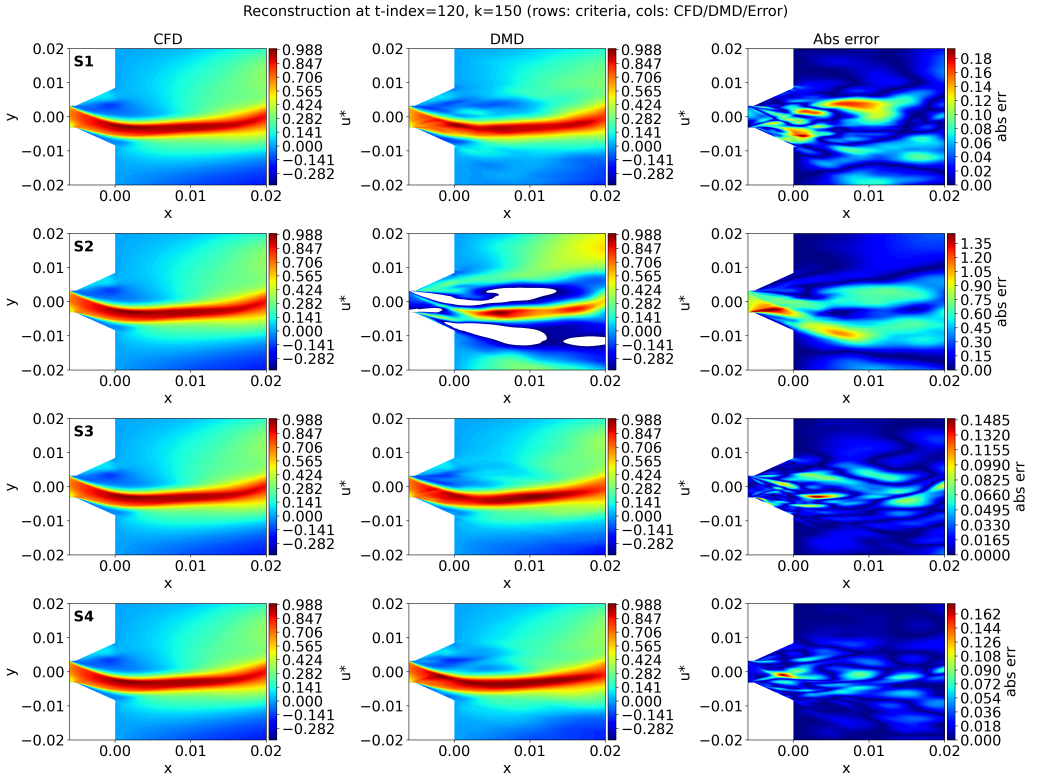


Figure 4. Effect of different DMD mode selection criteria on instantaneous velocity-field reconstruction for the baseline case ($\dot{m} = 0.01$ lb/s, $f = 263.5$ Hz, $r = 150$) at t-index $= 120$. Columns show the reference CFD field, DMD reconstructions, and absolute error. Rows correspond to the four criteria: amplitude-based sorting (S1), amplitude weighted by growth/decay (S2), amplitude integrated over time (S3), and ES-DMD eigenvalue-based sorting (S4). The variable u^* denotes the normalized velocity.

As shown in Figure 4, ES-DMD (S4) yields smooth, physically consistent reconstructions across the domain, accurately capturing both jet deflection and shear-layer intensity.

Figure 5 highlights the distinction of ES-DMD (S4). While amplitude-based criteria distribute selected modes broadly across the eigenspectrum, ES-DMD (S4) concentrates on eigenvalues near the unit circle, which correspond to persistent oscillatory behavior. This eigenspectrum bias is particularly beneficial for the higher-frequency baseline case, where preserving sustained oscillatory content is essential to reconstruct the rapid switching dynamics without introducing transient drift.

The dominant ES-DMD (S4) modes and their time dynamics shown in Figures 6 and 7, respectively, further confirm the physical relevance of the extracted structures. The leading mode captures the mean jet profile, while higher-order modes correspond to coherent

oscillatory components responsible for jet sweeping. The imaginary parts of the associated eigenvalues encode oscillation frequencies, while the real parts represent growth or decay rates. Near-zero real parts, therefore, indicate sustained dynamics.

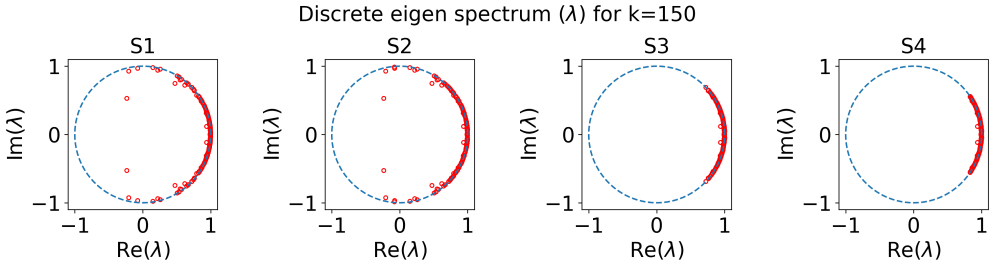


Figure 5. DMD eigenvalue distributions for the four mode selection criteria using $r = 150$ retained modes for the baseline case ($\dot{m} = 0.01$ lb/s). Blue dashed circle indicates the unit circle ($|\lambda| = 1$), and the red markers denote the computed DMD eigenvalues. ES-DMD (S4) preferentially selects modes clustered near the unit circle ($|\lambda| \approx 1$), corresponding to near-neutrally stable dynamics that persist over repeated switching cycles.

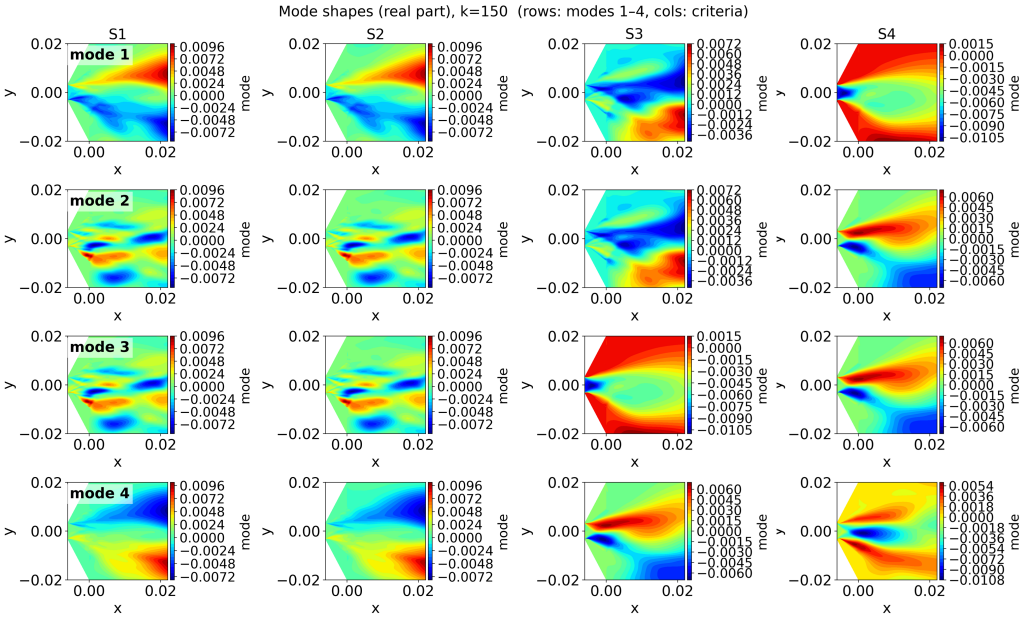


Figure 6. First four DMD mode shapes (real part) for each criterion (rows: modes 1–4, columns: S1–S4) for the baseline case with $r = 150$. The leading mode represents the mean-like structure, while higher-order modes encode oscillatory switching features.

4.2. Sensitivity to Time Step Selection

The sensitivity of ES-DMD to temporal resolution is evaluated using three time steps: $\Delta t_1 = 2 \times 10^{-5}$ s, $\Delta t_2 = 5 \times 10^{-5}$ s, and $\Delta t_3 = 1 \times 10^{-4}$ s. For the baseline frequency ($f = 263.5$ Hz), these correspond to approximately 190, 76, and 38 samples per oscillation period, respectively.

As shown in Figure 8, ES-DMD (S4) accurately reconstructs the oscillatory signal during the training window and maintains stable short-term prediction for a fraction of the subsequent period across all time steps. This prediction horizon is sufficient for boundary-condition applications in coupled simulations, where the ROM is evaluated repeatedly over short macro-time steps.

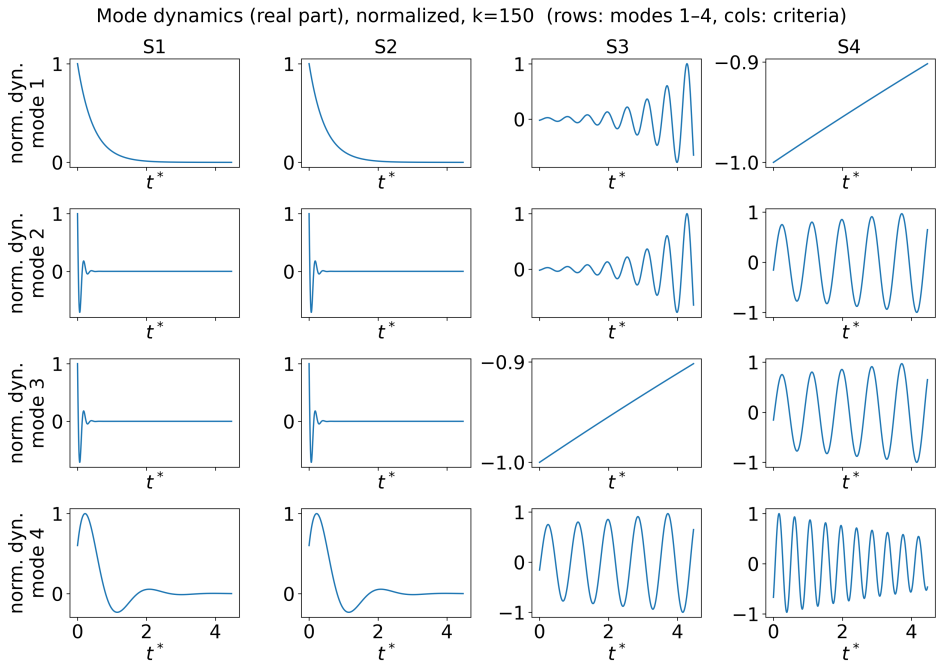


Figure 7. Normalized time dynamics (real part) of the first four retained modes for each criterion (rows: modes 1–4, columns: S1–S4) for the baseline case with $r = 150$. ES-DMD (S4) retains temporally persistent oscillatory dynamics associated with switching.

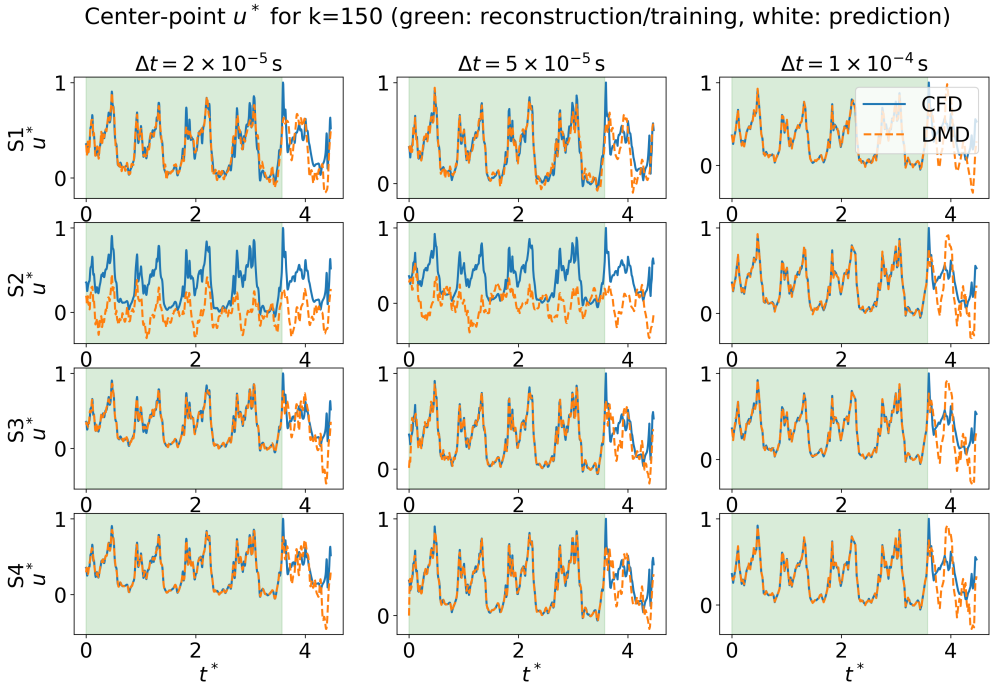


Figure 8. Normalized streamwise velocity u^* at the center point for different time steps with $r = 150$ (rows: criteria, columns: Δt). Green shading indicates reconstruction (training window), while the white region denotes prediction. ES-DMD (S4) maintains stable reconstruction and short-term prediction across temporal resolutions.

Figure 9 quantifies global reconstruction accuracy using

$$\mathrm{RMSE} = \sqrt{\frac{1}{N}\sum_{j=1}^{N}(Y_{\mathrm{CFD},j} - Y_{\mathrm{DMD},j})^2}. \tag{9}$$

During the reconstruction window, ES-DMD (S4) maintains consistently low RMSE relative to the alternative criteria. Across all time steps, prediction errors increase beyond the training window, but ES-DMD (S4) exhibits controlled growth and avoids the elevated error levels observed for criteria that over-weight transient or non-persistent contributions.

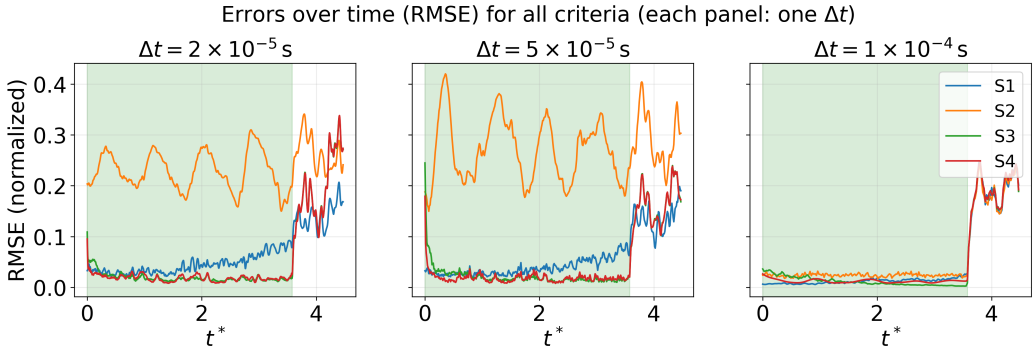


Figure 9. Errors over time (RMSE) for all four criteria at each time step (each panel: one Δt). Green shading indicates reconstruction (training window), while the white region denotes prediction.

4.3. Performance Across Operating Frequencies

The robustness of ES-DMD (S4) across operating conditions is assessed for three mass flow rates corresponding to oscillation frequencies of 65.9 Hz, 131.8 Hz, and 263.5 Hz.

As shown in Figure 10, ES-DMD (S4) maintains accurate reconstruction and stable short-term prediction across the frequency range. To achieve approximately 90% reconstruction accuracy, the required fraction of retained modes increases with frequency: 13% at 65.9 Hz, 38% at 131.8 Hz, and 55% at 263.5 Hz (baseline). This trend reflects increasing dynamical complexity at higher switching rates, introducing sharper transitions and richer temporal content that require additional modes of representation.

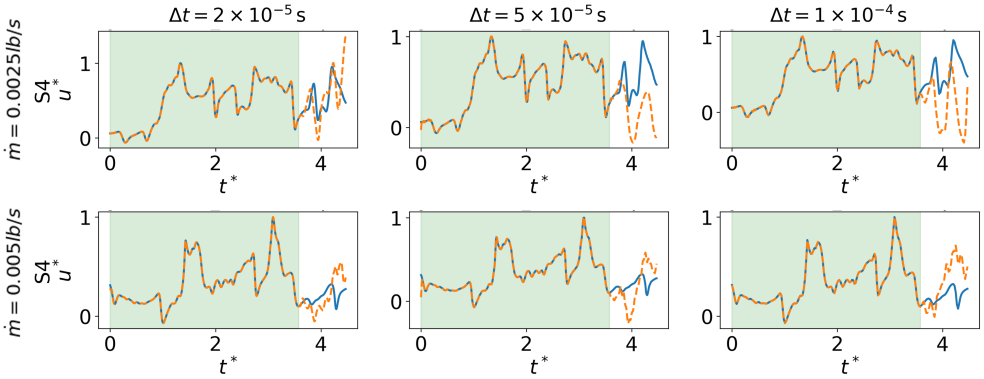


Figure 10. Center-point normalized velocity u^* showing ES-DMD (S4) reconstruction and prediction at lower mass flow rates. The green region indicates reconstruction, and the white region indicates prediction. The cases shown correspond to $\dot{m} = 0.0025$ lb/s ($f = 65.9$ Hz) and $\dot{m} = 0.005$ lb/s ($f = 131.8$ Hz).

Notably, the baseline case at $\dot{m} = 0.01$ lb/s corresponds to an exit Mach number of 0.34. The successful reconstruction under these conditions indicates that ES-DMD (S4) remains stable and effective in moderately compressible regimes, where switching dynamics are faster, and gradients are stronger.

4.4. Boundary Condition Generation from One-Dimensional Profiles

The primary aerospace objective of the proposed framework is to generate compact, predictive boundary conditions. ES-DMD (S4) is applied to one-dimensional exit-plane profiles and combined with time-delay embedding using $l = 400$ delays.

Figure 11 shows that with only 20 modes (7.6% of the full system rank), the prediction quality depends strongly on the mode-ranking strategy: ES-DMD (S4) better preserves the oscillatory structure and phase compared to criteria that emphasize transient or non-persistent contributions. Increasing the number of modes improves performance across criteria, with ES-DMD maintaining the most consistent behavior during both reconstruction and prediction.

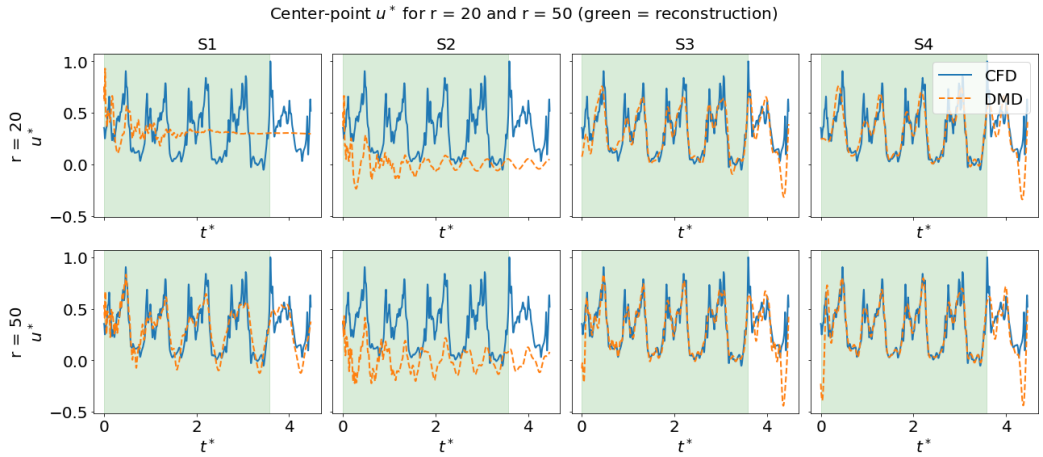


Figure 11. Center-point u^* prediction for reduced ranks $r = 20$ and $r = 50$ (rows: r, columns: criteria). Green shading indicates reconstruction (training window). The plots show the sensitivity of prediction quality to retained rank for each sorting criterion.

Figure 12 demonstrates that ES-DMD (S4) combined with time-delay embedding enables accurate multi-period prediction of both velocity and pressure using a minimal number of modes. The model reproduces the dominant oscillation peaks and phase during reconstruction and maintains stable oscillatory behavior into the prediction window, supporting its intended use as a time-resolved boundary-condition generator. Compared to the 150 modes required for comparable two-dimensional field reconstruction, this represents a substantial reduction in model complexity.

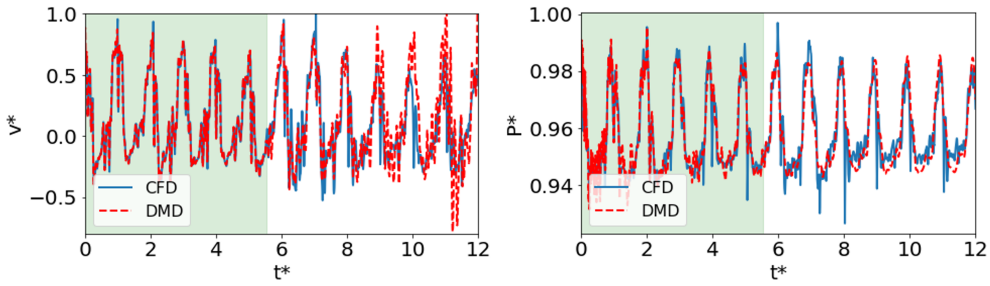


Figure 12. Simultaneous prediction of normalized velocity and pressure signals at the center point using ES-DMD (S4) with time-delay embedding. The green region indicates reconstruction, and the white region indicates prediction.

The enhanced performance arises from the complementary roles of time-delay embedding, which enriches temporal dynamics for low-dimensional boundary signals, and ES-DMD, which focuses the augmented state space on physically meaningful, sustained oscillatory modes. This synergy yields a compact and robust boundary-condition model suitable for integration into large-scale aerospace CFD simulations.

4.5. Discussion and Practical Implications

The results demonstrate that ES-DMD mitigates several persistent challenges in reduced-order modeling of high-frequency sweeping jet actuators. Conventional amplitude-based mode selection can under-represent dynamically important switching behavior when those dynamics are not associated with the largest initial modal amplitudes. ES-DMD addresses this by ranking modes using discrete-time eigenvalue information, favoring eigenvalues with larger real parts clustered near the unit circle ($\Re(\lambda) \approx 1$), which correspond to near-neutrally stable dynamics that persist across multiple oscillation cycles and therefore better represent sustained switching behavior.

A key practical outcome is robustness across both temporal discretization and operating conditions. ES-DMD maintains consistent reconstruction accuracy over the tested time steps (Figures 8 and 9), and preserves stable reconstruction and short-term prediction across the full frequency range (Figure 10). The observed increase in required mode count with frequency (13% at 65.9 Hz to 55% at 263.5 Hz for ≈90% reconstruction accuracy) provides direct guidance for ROM dimensioning: higher-frequency operation introduces sharper transitions and richer temporal content, requiring more modes to represent the dynamics at comparable fidelity. Notably, the baseline case at 263.5 Hz corresponds to an exit Mach number of 0.34, indicating that the method remains stable and effective in moderately compressible regimes with stronger gradients and faster switching.

The prediction horizon depends strongly on whether the ROM is built from full-field snapshots or from one-dimensional exit profiles with time-delay embedding. For the two-dimensional field reconstructions, predictions beyond the training interval remain limited (approximately a fraction of a period in Figure 8), consistent with the limitations of linear DMD models for representing nonlinear dynamics with exponential evolution. In contrast, when ES-DMD is applied to one-dimensional exit-plane profiles using Hankel time-delay embedding, the ROM achieves stable multi-period predictions for both velocity and pressure with only 20 modes (Figure 12). It indicates that temporal embedding substantially improves predictability for the low-dimensional boundary-condition signals, which are the primary quantities of interest for coupled aerospace simulations.

From an aerospace integration perspective, the most significant implication is the demonstrated feasibility of replacing actuator-resolved unsteady CFD with a compact boundary-condition ROM. The ability to reproduce exit dynamics using a 1D profile model with only 20 modes (7.6% of the full system rank) supports a multiscale simulation workflow in which actuator unsteadiness is represented efficiently. At the same time, the global configuration is solved using RANS. This approach avoids the prohibitive cost of resolving actuator-scale geometry and time steps on full-configuration grids, while retaining the unsteady switching signatures needed for meaningful assessment of active flow control.

Finally, the successful application at the highest tested operating condition, $f = 263.5$ Hz ($St = 0.014$, exit Mach 0.34), demonstrates that the framework remains effective at frequencies beyond many commonly reported SJA ROM demonstrations. Coupled with the demonstrated mode efficiency for boundary-condition generation, these results position ES-DMD as a practical reduced-order modeling tool for embedding the effects of sweeping jet actuators into full-scale aerodynamic simulations.

5. Conclusions

This study developed and validated an Eigenvalue-Sorted Dynamic Mode Decomposition (ES-DMD) framework tailored for reduced-order modeling of high-frequency sweeping jet actuators (SJAs) in aerospace active flow control applications. The primary contributions and findings are summarized as follows:

1. Stability-aware mode selection: ES-DMD introduces a stability-based sorting strategy that ranks modes using discrete-time DMD eigenvalues, prioritizing eigenvalues with larger real parts clustered near the unit circle ($\Re(\lambda) \approx 1$), which correspond to near-neutrally stable oscillatory dynamics, rather than large initial amplitudes. This approach more reliably captures the sustained switching behavior of high-frequency SJAs compared to conventional amplitude-based criteria.
2. Robust performance across operating conditions: The proposed method demonstrates consistent reconstruction accuracy across a broad range of operating frequencies (65.9–263.5 Hz) and temporal resolutions (2×10^{-5}–1×10^{-4} s). As oscillation frequency increases, a larger fraction of modes is required to represent the enhanced dynamical complexity (55% at 263.5 Hz versus 13% at 65.9 Hz). Yet, ES-DMD remains stable and accurate throughout the tested range. Notably, the highest-frequency case (263.5 Hz) corresponds to an exit Mach number of 0.34, indicating that the framework remains effective in moderately compressible regimes with stronger gradients and faster switching.
3. Efficient boundary-condition modeling: When combined with time-delay embedding, ES-DMD enables accurate reconstruction and multi-period prediction of one-dimensional exit-plane velocity and pressure profiles using only 20 modes (7.6% of the full system rank). This compact representation is sufficient to generate time-resolved boundary conditions suitable for coupled aerodynamic simulations.
4. Improved accuracy over established criteria: Direct comparison with three commonly used DMD mode selection strategies shows that ES-DMD consistently yields lower reconstruction errors and smoother, more physically interpretable flow fields for oscillatory SJA dynamics. The stability-aware sorting avoids the localized artifacts observed in amplitude-weighted and time-integrated criteria for this dataset.

From an aerospace modeling perspective, the principal implication of this work is the ability to integrate high-frequency SJA effects into large-scale aerodynamic simulations without resolving actuator-scale geometry or time steps. By replacing actuator-resolved unsteady CFD with a compact, physics-informed reduced-order boundary condition, ES-DMD enables efficient multiscale simulation workflows compatible with RANS-based full-configuration analyses.

Future work will extend the framework to three-dimensional actuator configurations, investigate nonlinear extensions via operator inference or hybrid data-driven models, and validate the proposed boundary-condition strategy in coupled actuator–airfoil simulations. The ES-DMD framework thus provides a practical, data-driven pathway to integrate the dynamic effects of fluidic actuators into the computational design and analysis cycles of next-generation AFC-equipped aerospace vehicles.

Author Contributions: Conceptualization, S.A.S.R., M.A. and K.K.; methodology, K.K., M.A. and S.A.S.R.; validation, M.A. and S.A.S.R., formal analysis, M.A., S.A.S.R. and K.K.; investigation, M.A., S.A.S.R. and K.K.; resources, K.K.; writing—original draft preparation, S.A.S.R. and M.A.; writing—review and editing, S.A.S.R., M.A. and K.K.; visualization, M.A., S.A.S.R. and K.K.; supervision, K.K.; project administration, K.K.; funding acquisition, K.K. All authors have read and agreed to the published version of the manuscript.

Funding: This research received no external funding.

Institutional Review Board Statement: In this study, no human or animal has been involved.

Data Availability Statement: The data in this study is available from the corresponding author upon request.

Conflicts of Interest: The authors declare no conflicts of interest.

Abbreviations

The following abbreviations are used in this manuscript:

Symbol	Description
AFC	Active Flow Control
CFD	Computational Fluid Dynamics
DES	Detached Eddy Simulation
DMD	Dynamic Mode Decomposition
ES-DMD	Eigenvalue-Sorted Dynamic Mode Decomposition
LES	Large Eddy Simulation
ROM	Reduced-Order Model
RANS	Reynolds-Averaged Navier–Stokes
RMSE	Root Mean Square Error
SJA	Sweeping Jet Actuator
SVD	Singular Value Decomposition
URANS	Unsteady Reynolds-Averaged Navier–Stokes
C_μ	Momentum Coefficient
f	Frequency (Hz)
$\dot{m}$	Mass flow rate
Re	Reynolds number
St	Strouhal number

References

1. Lin, J.C.; Andino, M.Y.; Alexander, M.G.; Whalen, E.A.; Spoor, M.A.; Tran, J.T.; Wygnanski, I.J. An overview of active flow control enhanced vertical tail technology development. In Proceedings of the 54th AIAA Aerospace Sciences Meeting, San Diego, CA, USA, 4–8 January 2016; AIAA 2016-0056 .
2. Pack Melton, L.G.; Koklu, M. Active flow control using sweeping jet actuators on a semi-span wing model. In Proceedings of the 54th AIAA Aerospace Sciences Meeting, San Diego, CA, USA, 4–8 January 2016; AIAA 2016-1817.
3. Kara, K.; Kim, D.; Morris, P.J. Flow-separation control using sweeping jet actuator. *AIAA J.* **2018**, *56*, 4604–4613. [CrossRef]
4. Graff, E.; Seele, R.; Lin, J.C.; Wygnanski, I. *Sweeping Jet Actuators—A New Design Tool for High Lift Generation*; Technical Report; Langley Research Center: Hampton, VA, USA, 2013.
5. Andino, M.Y.; Lin, J.C.; Washburn, A.E.; Whalen, E.A.; Graff, E.C.; Wygnanski, I.J. Flow separation control on a full-scale vertical tail model using sweeping jet actuators. In Proceedings of the 53rd AIAA Aerospace Sciences Meeting, Kissimmee, FL, USA, 5–9 January 2015; AIAA 2015-0785.
6. Intravartolo, N.; Miller, A.; Woszidlo, R.; Phillips, E.; Shmilovich, A. Development of Active Flow Control Prediction Tools for Aircraft Conceptual Design. In Proceedings of the AIAA SCITECH 2023 Forum, National Harbor, MD, USA; Online, 23–27 January 2023; AIAA 2023-2310.
7. Ho, H.H.; Shirinzad, A.; Essel, E.E.; Sullivan, P.E. Synthetic jet actuators for active flow control: A review. *Fluids* **2024**, *9*, 290. [CrossRef]
8. Andino, M.Y.; Pack Melton, L.G.; Koklu, M.; Hannon, J. Active Flow Control Enhanced Aileron of the High-Lift Common Research Model at Takeoff Condition. In Proceedings of the AIAA SCITECH 2025 Forum, Orlando, FL, USA, 6–10 January 2025; AIAA 2025-1491.
9. Childs, R.E.; Stremel, P.M.; Kushner, L.K.; Heineck, J.T.; Storms, B.L. Simulation of sweep-jet flow control, single jet and full vertical tail. In Proceedings of the 54th AIAA Aerospace Sciences Meeting, San Diego, CA, USA, 4–8 January 2016; AIAA 2016-0569.
10. Vijgen, P.M.; Ziebart, A.; Shmilovich, A.; Woszidlo, R. Conceptual Integration Studies of Localized Active Flow Control on the Wing of a Commercial Aircraft. In Proceedings of the AIAA SCITECH 2023 Forum, National Harbor, MD, USA; Online, 23–27 January 2023; AIAA 2023-0657.
11. Kara, K. Numerical simulation of a sweeping jet actuator. In Proceedings of the 34th AIAA Applied Aerodynamics Conference, Washington, DC, USA, 13–17 June 2016; AIAA 2016-3261.
12. Koklu, M. Effects of sweeping jet actuator parameters on flow separation control. *AIAA J.* **2018**, *56*, 100–110. [CrossRef] [PubMed]
13. Slupski, B.J.; Tajik, A.R.; Parezanović, V.B.; Kara, K. On the Impact of Geometry Scaling and Mass Flow Rate on the Frequency of a Sweeping Jet Actuator. *FME Trans.* **2019**, *47*, 599–607. [CrossRef]

14. Chapin, V.; Bénard, E. Active control of a stalled airfoil through steady or unsteady actuation jets. *J. Fluids Eng.* **2015**, *137*, 091103. [CrossRef]
15. Rumsey, C.L.; Coleman, G.N.; Wang, L. In search of data-driven improvements to RANS models applied to separated flows. In Proceedings of the AIAA Scitech 2022 Forum, San Diego, CA, USA, 3–7 January 2022; AIAA 2022-0937.
16. Vatsa, V.N.; Duda, B.M.; Lin, J.C.; Pack Melton, L.G.; Lockard, D.P.; O'Connell, M.; Hannon, J. Comparative study of active flow control strategies for lift enhancement of a simplified high-lift configuration. In Proceedings of the AIAA Aviation 2019 Forum, Dallas, TX, USA, 17–21 June 2019; AIAA 2019-3724.
17. Takken, M.; Wille, R. Accelerated Computational Fluid Dynamics Simulations of Microfluidic Devices by Exploiting Higher Levels of Abstraction. *Micromachines* **2024**, *15*, 129. [CrossRef]
18. Yamaleev, N.K.; Carpenter, M.H.; Ferguson, F. Reduced-order model for efficient simulation of synthetic jet actuators. *AIAA J.* **2005**, *43*, 357–369. [CrossRef]
19. Pasquetti, R.; Peres, N. A penalty model of synthetic micro-jet actuator with application to the control of wake flows. *Comput. Fluids* **2015**, *114*, 203–217. [CrossRef]
20. Radespiel, R.; Burnazzi, M.; Casper, M.; Scholz, P. Active flow control for high lift with steady blowing. *Aeronaut. J.* **2016**, *120*, 171–200. [CrossRef]
21. Schmid, P.J. Dynamic mode decomposition of numerical and experimental data. *J. Fluid Mech.* **2010**, *656*, 5–28. [CrossRef]
22. Kutz, J.N.; Brunton, S.L.; Brunton, B.W.; Proctor, J.L. *Dynamic Mode Decomposition: Data-Driven Modeling of Complex Systems*; Society for Industrial and Applied Mathematics: Philadelphia, PA, USA, 2016.
23. Schmid, P.J.; Li, L.; Juniper, M.P.; Pust, O. Applications of the dynamic mode decomposition. *Theor. Comput. Fluid Dyn.* **2011**, *25*, 249–259.
24. Chen, S.; Tu, T.; Zeng, C.; Meng, Q. Modal analysis of compressor cascades with sweeping jet actuator and pulsed jet for active flow control based on large Eddy simulation. *Aerosp. Sci. Technol.* **2022**, *131*, 107997. [CrossRef]
25. Amitay, M.; Glezer, A. Role of actuation frequency in controlled flow reattachment over a stalled airfoil. *AIAA J.* **2002**, *40*, 209–216. [CrossRef]
26. Wen, X.; Tang, H.; Duan, F. Vortex dynamics of in-line twin synthetic jets in a laminar boundary layer. *Phys. Fluids* **2015**, *27*, 083601. [CrossRef]
27. Sieber, M.; Paschereit, C.O.; Oberleithner, K. Spectral proper orthogonal decomposition. *J. Fluid Mech.* **2016**, *792*, 798–828. [CrossRef]
28. Towne, A.; Schmidt, O.T.; Colonius, T. Spectral proper orthogonal decomposition and its relationship to dynamic mode decomposition and resolvent analysis. *J. Fluid Mech.* **2018**, *847*, 821–867. [CrossRef]
29. Kou, J.; Zhang, W. An improved criterion to select dominant modes from dynamic mode decomposition. *Eur. J. Mech. B/Fluids* **2017**, *62*, 109–129.
30. Schmid, P.J. Dynamic mode decomposition and its variants. *Annu. Rev. Fluid Mech.* **2022**, *54*, 225–254. [CrossRef]
31. Ahmed, S.E.; Dabaghian, P.H.; San, O.; Bistrian, D.A.; Navon, I.M. Dynamic mode decomposition with core sketch. *Phys. Fluids* **2022**, *34*, 066603. [CrossRef]
32. Tu, J.H. Dynamic Mode Decomposition: Theory and Applications. Ph.D. Thesis, Princeton University, Princeton, NJ, USA, 2013.
33. Yuan, Y.; Zhou, K.; Zhou, W.; Wen, X.; Liu, Y. Flow prediction using dynamic mode decomposition with time-delay embedding based on local measurement. *Phys. Fluids* **2021**, *33*, 095109. [CrossRef]
34. Kara, K. Numerical study of internal flow structures in a sweeping jet actuator. In Proceedings of the 33rd AIAA Applied Aerodynamics Conference, Dallas, TX, USA, 22–26 June 2015; AIAA 2015-2424.
35. Slupski, B.Z.; Kara, K. Effects of geometric parameters on performance of sweeping jet actuator. In Proceedings of the 34th AIAA Applied Aerodynamics Conference, Washington, DC, USA, 13–17 June 2016; AIAA 2016-3263.
36. Alam, M.; Kara, K. The influence of exit nozzle geometry on sweeping jet actuator performance. *Fluids* **2022**, *7*, 69. [CrossRef]
37. ANSYS, Inc. *ANSYS Fluent User Guide*; Version 2021.R2; ANSYS, Inc.: Canonsburg, PA, USA, 2021.
38. Menter, F.R. Two-equation eddy-viscosity turbulence models for engineering applications. *AIAA J.* **1994**, *32*, 1598–1605.
39. Oz, F.; Kara, K. Jet oscillation frequency characterization of a sweeping jet actuator. *Fluids* **2020**, *5*, 72. [CrossRef]
40. Askham, T.; Kutz, J.N. Variable projection methods for an optimized dynamic mode decomposition. *Siam J. Appl. Dyn. Syst.* **2018**, *17*, 380–416.
41. Liu, Y.; Long, J.; Wu, Q.; Huang, B.; Wang, G. Data-driven modal decomposition of transient cavitating flow. *Phys. Fluids* **2021**, *33*, 113316. [CrossRef]
42. Gilotte, P.; Mortazavi, I.; Edwige, S. Active control and modal decomposition for the flow over a ramp. *Int. J. Heat Fluid Flow* **2024**, *107*, 109374. [CrossRef]
43. Frame, P.; Towne, A. Space-time POD and the Hankel matrix. *PLoS ONE* **2023**, *18*, e0289637.
44. Dylewsky, D.; Kaiser, E.; Brunton, S.L.; Kutz, J.N. Principal component trajectories for modeling spectrally continuous dynamics as forced linear systems. *Phys. Rev. E* **2022**, *105*, 015312. [CrossRef]

45. Nedzhibov, G. Delay-embedding spatio-temporal dynamic mode decomposition. *Mathematics* **2024**, *12*, 762.
46. Ahmed, S.E.; San, O.; Bistrian, D.A.; Navon, I.M. Sampling and resolution characteristics in reduced order models of shallow water equations: Intrusive vs nonintrusive. *Int. J. Numer. Methods Fluids* **2020**, *92*, 992–1036. [CrossRef]

Disclaimer/Publisher's Note: The statements, opinions and data contained in all publications are solely those of the individual author(s) and contributor(s) and not of MDPI and/or the editor(s). MDPI and/or the editor(s) disclaim responsibility for any injury to people or property resulting from any ideas, methods, instructions or products referred to in the content.